PREPRINT - GPU-based Static Optimal Control: Real-Time Optimization within Closed-Loop Aim Point Control for Solar Power Towers

Laurin Oberkirsch[a,∗], David Zanger[a], Daniel Maldonado Quinto[a], Peter Schwarzbözl[a], Bernhard Hoffschmidt[a]

[a]German Aerospace Center (DLR), Institute of Solar Research, Linder Höhe, D-51147 Köln, Germany

Abstract

Many aim point optimization techniques exist to control *Solar Power Towers* (SPTs). However, SPTs exhibit optical losses that cannot be exactly modeled. Moreover, cloud passages cause transient incident flux distributions. Due to these modeling errors and disturbances, aim point optimization may exceed the *Allowable Flux Density* (AFD); consequently, these efficient aiming strategies are seldom applied at commercial plants. In this paper, an innovative closed-loop aim point control technique, the *Static Optimal Control*, is proposed. Flux density measurements close the open control loop of aim point optimization. Based on this feedback, the Static Optimal Control estimates weights that are embedded in the cost function of the aim point optimization. This GPU-based optimizer finds good aim point configurations in a few seconds even for large plants. Thus, the Static Optimal Control compensates for modeling errors and rejects disturbances to observe the AFD while maximizing the intercept. The performance of the Static Optimal Controller is evaluated for inaccurately modeled mirror errors and under a real cloud scenario. Aim of this control is not to exceed the AFD by more than 5 % i.e. the accuracy of the flux density measurements. The aim is achieved for static modeling errors while improving the intercept by 1.7-8.6 % compared to a heuristic control. In the cloud scenario, the Static Optimal Control reaches its limits. Even mapping all-sky-imager-based nowcasts in a feed forward manner on the heliostat field does not improve the control quality due to high prediction errors.

Keywords: Concentrating solar power, Solar power tower, Heliostat aiming, Aim point optimization, Optimal control, Cloud disturbance

1. Introduction

One of the first aiming strategies for *Solar Power Tower* (SPT) plants is the combination of static and dynamic aim point processing system. Vant-Hull et al. (1996a,b) developed it for the molten salt central receiver in the Solar Two Project (Smith, 1992; Bradshaw et al., 2002). While the *Static Aimpoint Processing System* (SAPS) is an open-loop control that distributes the aim points for each heliostat, the *Dynamic Aimpoint Processing System* (DAPS) is rather a closed-loop control that reduces the allocated heliostats at aim points with flux excess.

The DAPS detects "hot spots" exceeding the *Allowable Flux Density* (AFD) (Vant-Hull, 2002) and eliminates them. The AFD is the minimum of the limit due to thermal stresses and the limit due to salt corrosion. It is determined based on local salt temperature and velocity. Moreover, only the heliostat field, but not the receiver is actively controlled. First, the system identifies the receiver bin with the highest exceedance of the AFD. Subsequently, the heliostat causing based on the simulation model the highest flux in this bin is defocused. This procedure re-peats until the flux density complies with the AFD for each hot spot (Vant-Hull et al., 1996a).

The SAPS spreads as heuristic method the aim points vertically from the receiver's edges depending on the heliostats' beam radii (Vant-Hull et al., 1996a,b). In the recent years, the SAPS is continuously extended: Sánchez-González and Santana (2015); Sánchez-González et al. (2017, 2018) introduced the aiming factor k, Flesch et al. (2017) and Collado and Guallar (2019) segmented the field in radial sectors, Vant-Hull et al. (1996b) and Sánchez-González et al. (2017) in azimuthal sectors and Astolfi et al. (2017) and García et al. (2017) merged radial and azimuthal approach. Due to all these improvements, the maximal flux density reduces further and the efficiency increases slightly.

Since the computational power rose in the past, more and more meta-heuristic approaches like TABU algorithms (Salomé et al., 2013; Yu et al., 2014; Grange and Flamant, 2021) or genetic algorithms (Besarati et al., 2014; Wang et al., 2017; Cruz et al., 2018, 2019; Zhu and Ni, 2019) are applied to solve the combinatorial NP-complete knapsack problem (Kellerer et al., 2004) of assigning heliostats to pre-defined aim points on the surface of the receiver. Even, *Binary Integer Linear Programming* (BILP) (Ashley et al., 2017) and *Mixed Integer Linear Program-*

---

ming (MILP) (Richter et al., 2019) algorithms coupled with a Gamma robustness approach to cover uncertainties (Kuhnke et al., 2020) are evaluated. By applying grouping and aim point reduction strategies, the run time can even be reduced down to 10 s for large heliostat fields by using twelve cores in parallel (Speetzen and Richter, 2021).

Moreover, Belhomme et al. (2013) adapted the *Ant-Colony Optimization* (ACO) meta-heuristic to maximize the intercept. While it complies with the AFD for arbitrary receiver types, this method improves the single factor aiming by 2 % for cylindrical receivers (Flesch et al., 2017). When this method is coupled with a local search algorithm, it reaches faster convergence (Maldonado et al., 2018). Oberkirsch et al. (2021) improved the computational speed of the ACO algorithm by grouping the heliostats based on k-means clustering and by porting it to the GPU.

Clouds can shade even large heliostat fields in less than 5 min assuming mean cloud speeds in southern Spain of 7.36 m s^{-1} (Kuhn et al., 2018). Even under these transient conditions aim point optimization can determine near optimal solutions as cloud predictions can be included in the system model. There, the optimization requires around 30 s (Ashley et al., 2017; Oberkirsch et al., 2021) matching the temporal resolution of *All-Sky-Imager* (ASI)-based nowcasting systems (Nouri et al., 2018, 2019, 2020).

However, these open-loop controllers cannot compensate for modeling errors due to inaccurately estimated tracking or mirror errors nor reject other disturbances like uncertainties in the cloud prediction. Hence, a real plant requires, next to an open-loop aim point control, a closed-loop aim point control. Similar to Vant-Hull et al. (1996a), who coupled SAPS with DAPS, Cruz et al. (2019, 2020) added a heuristic control downstream of the genetic algorithm. This heuristic activates and deactivates heliostats and shifts iteratively heliostats from spots, that exceed the AFD, to spots with a low flux density. Similarly, García-Martín et al. (1999) shifts heliostats to control the receiver's temperature at the PSA's CESA-1 plant. There, not only the heliostats move from aim points in hot regions to aim points in cold regions, but also the aim points itself wander to balance the flux distribution within the vicinity of the aimpoint.

A different approach is proposed by García et al. (2017), who decouple the *Multi-Input Multi-Output* (MIMO) system into 54 *Single-Input Single-Output* (SISO)

subsystems. Each subsystem describes a group of heliostats and is controlled by a *Proportional Integral Derivative* (PID) controller. The PID controller adjusts dispersion and position of the group's aim points for cylindrical receivers (García et al., 2018). Acosta et al. (2021) already applied the approach to the reference power plant used in this work (Flesch et al., 2017) and used a raytracer instead of the HFLCAL convolution method (Schwarzbözl et al., 2009) as radiation model. García et al. (2018) and Soo Too et al. (2019) replaced the PID controllers by a *Model Predictive Controller* (MPC), called *Dynamic Matrix Control* (DMC) and exposed the plant to transient conditions. To overcome overshoots in the flux density, they added a *Proportional Integral* (PI) controller to successively readjust the setpoint flux after the cloud has passed. By including the slant range between heliostat and tower, this control strategy is simplified to one that requires only one manipulated variable per panel (García et al., 2020) and a tuning analysis is performed (García et al., 2022).

Up to now, the flux density demand for closed-loop aim point controls is usually determined based on temperature measurements and a thermal model (Gross et al., 2020). The *Aim Point Strategy* (APS) of Gross et al. (2020) accomplishes to meet this demand with a deviation of less than $150\,\mathrm{kW\,m^{-2}}$ in either direction. In this work, we assume a directly measured incidence flux density distribution on the receiver surface as feedback for the closed-loop control. Several techniques like moving bars or direct flux measurements using the receiver's reflection can provide these solar flux density distribution even for large-scale receivers. However, moving bars are disadvantageous due to large moving parts and direct measurements may be less precise (Röger et al., 2014). Therefore, Offergeld et al. (2019) enhanced the direct flux density measurement system of Göhring et al. (2011) by developing the scan method. In this way, accuracies of 2-9 % are achieved (Stadler et al., 2019).

In this work, we present a closed-loop aim point control strategy: the Static Optimal Control. Aim of the Static Optimal Control is to find solutions that exceed the AFD by less than the accuracy of the measurement system. Thus, 5 % are selected as a mean accuracy between 2-9 % (Stadler et al., 2019). To maximize the intercept while compensating for modeling errors and disturbances, the Static Optimal Control embeds the ACO meta-heuristic (Belhomme et al., 2013). This ACO algorithm was enhanced by Oberkirsch et al. (2021) to achieve the required convergence rate for the application in the Static Optimal Control. Finally, the control quality of the Static Optimal Control is evaluated under different scenarios at a plant of commercial scale.

2. Methods

Since the aim point optimization is the heart of the *Static Optimal Control* it is introduced first in this section. Both, the basic ACO meta-heuristic as well as some

improvements are described. Afterwards, the controller comprising error signal calculator, weight calculator, anti wind up, optimizer, objective function and objective value scaler is presented in detail.

2.1. Aim point optimization

Ant-colony optimization meta-heuristic: During foraging, ants communicate through emitting pheromones and build a swarm intelligence. This multi-agent method is adapted by Belhomme et al. (2013) to maximize the intercept of SPT plants. While each ant describes a certain path in reality, each ant evaluates a certain aim point configuration in this analogy. An aim point configuration characterizes one specific allocation of all heliostats to predefined aim points.

The path of an ant is determined by a probability and a random factor that is specified by a Monte-Carlo-Method. The probability is the product of pheromone concentration and attractiveness of a path, In reality, the ants emit pheromones; in consequence, the pheromone concentration alters. Moreover, the pheromones evaporate with time. Here, the concentration is regularly updated based on an objective value. The objective value used in this work is introduced in Section 2.2. Thus, the paths with greater objective values are favored and the evaporation prevents the algorithm to converge into local optima. The attractiveness of a path is the intercept of a heliostat assigned to an aim point. The intercept is the ratio of flux irradiating onto the receiver to the flux reaching the plane of the receiver.

Finally, all ants, each defining an aim point configuration, are evaluated and the best aim point configuration is selected. The corresponding best ant forms the next generation of ants.

The following sections describe three enhancements yielding a faster convergence of this ACO meta-heuristic:

1. Replacing raytracing by pre-calculated flux maps,
2. Clustering the heliostats to groups and
3. Porting the algorithm on the GPU.

Pre-calculated flux maps: One flux map is the emerging flux density distribution on the receiver's surface, when one heliostat points to one aim point. As the aim points are pre-defined on the surface of the receiver, raytracing and optimization can be decoupled by pre-calculating flux maps in advance.

The flux map varies both with the sun angle and the *Direct Normal Irradiance* (DNI). While the DNI scales the flux map only by a constant factor, the sun angle changes the shape of the flux map. Thus, the flux maps have to be pre-calculated for roughly 1830 sun angles in southern Spain to reach modeling errors below 1 % as analyzed by Oberkirsch et al. (2021). In this work, the raytracing is performed by the raytracing software $STRAL$[1].

---

[1] The *Solar Tower RAytracing Laboratory* (STRAL) is developed at the German Aerospace Center (Belhomme et al., 2009).

During optimization, the algorithm only superposes these pre-calculated flux maps instead of raytracing each aim point configuration. Thus, the computational time is reduced by factor $10^2 - 10^4$ as stated by Belhomme et al. (2013). The slight accuracy loss due to small errors in the modeling of shading and blocking is negligible for larger fields.

Grouping: In a next step, heliostats with similar focal spots are clustered into groups by the k-means clustering algorithm (Lloyd, 1982). As clustering parameters, the radius and the 2-argument arctangent *arctan2* are applied for circular heliostat fields as explained by Oberkirsch et al. (2021).

For each group, the flux maps of the contained heliostats are superposed and an overall flux map is stored. Thus, only the flux maps of all groups are superposed instead of superposing the flux maps of all heliostats when evaluating one aim point configuration. Moreover, the solution space S decreases clearly. In this way, the algorithm converges in less optimization steps and even less optimization time.

The effect of the group number is studied by Oberkirsch et al. (2021). The study exhibits faster convergence for a small number of groups, while better results are reached with more groups. In this work, 200 groups are evaluated as the strong convergence in the first seconds is important for the closed-loop aim point control.

At the same time, the required memory reduces by factor $10 - 100$ dependent on the average number of heliostats in a group. Only this memory reduction allows to shift all flux maps of a single sun angle into the GPU memory to achieve further optimization time reductions on the GPU.

GPU implementation: For the application in a closed-loop aim point control, the ACO meta-heuristic has to reach good solutions in short time. To achieve this, the algorithm is implemented in C for CUDA from NVIDIA (NVIDIA Corporation, 2019) by Oberkirsch et al. (2021) and runs on various CUDA-capable GPUs. The ACO meta-heuristic is well suited for this application due to its high degree of parallelization. This can be achieved as the individual ants can be computed perfectly parallelized. Thus, the algorithm profits significantly of the higher throughput on the GPU.

On a NVIDIA Quadro P5000, $50 \cdot 10^9$ flux values are evaluated per second including all overhead due to other operations during the optimization as Oberkirsch et al. (2021) determined. There, 1000 ant generation runs, each with 16384 ants, require 98 s when the ACO meta-heuristic is applied to a reference power plant. This reference power plant is also used in this work and later introduced in Section 3.1.

2.2. Static Optimal Control

The components of SPT plants contain several errors. Some of these errors like mirror or tracking errors can be modeled. However, the exact quantification of these errors is complicated. Thus, there is always a deviation between system model and reality. Moreover, the plant is exposed to disturbances. Some disturbances such as clouds can be predicted and included in the model. However, these disturbances still come with uncertainties. Hence, a closed-loop controller is necessary to compensate for modeling errors and disturbances; thus, feedback like measured flux maps is required.

The controlled optical system of an SPT plant has several thousand heliostats, each with a two-directional movement, as inputs and several thousand receiver bins as outputs. A receiver bin is a discrete element on the receiver surface. Hence, the optical system is a large MIMO system. Moreover, this optical system is non-linear and stable in every operating point. While the thermal side of the SPT plant exhibits long dynamics, the flux density distribution remains constant as soon as the heliostats have reached their orientation. Thus, the optical system can be considered static if the sample time is longer than the movement time of the heliostat to a new aim point. That means if the sample time covers all dynamics of the optical system. For the Cesa1 plant, the heliostat field requires less than 3 s for switching the aim point configuration when an angular velocity of $2\,°\,s^{-1}$ is assumed for the heliostats (Belhomme et al., 2013). Some suppliers even state angular velocities up to $12\,°\,s^{-1}$ (SENER, 2014).

Based on this system analysis, a closed-loop control is developed. To benefit from the fact that the optical system is considered static, the advantages of aim point optimization and the enhancements of the ACO meta-heuristic, the *Static Optimal Control* algorithm is proposed. The closed control loop including the Static Optimal Control is illustrated in Figure 1. The controller itself comprises the error signal calculator, the weight calculator and the optimizer. The controller is modular; thus, its individual components can be exchanged.

At the beginning of the control-loop, the error signal calculator determines based on the deviation between desired reference flux map $\mathbf{y}_{ref}$ and measured flux map $\mathbf{y}$ an error map $\mathbf{e}$ in each control step k. Based on this measured error, the weight calculator computes the weights of an objective function. In this way, the algorithm yields a solution with a reduced error.

To illustrate the workflow of the algorithm, Figure 2 presents the activity diagram of a single control step. In addition, a small example with two heliostats and three aim points demonstrates how the controller compensates a possible tracking error.

Initially, both heliostats point to the middle aim point 2. However, heliostat 2 exhibits a tracking error. Hence, it actually aims to aim point 3 leading to a shifted flux map. First, the flux map is measured and an error signal is calculated by subtracting the flux map from the reference flux map. Based on the scaled error map, the algorithm computes the weight map. As fluxes in bins with higher weights are preferred to maximize the objective function, the optimizer shifts the heliostats more to the left. Rea-
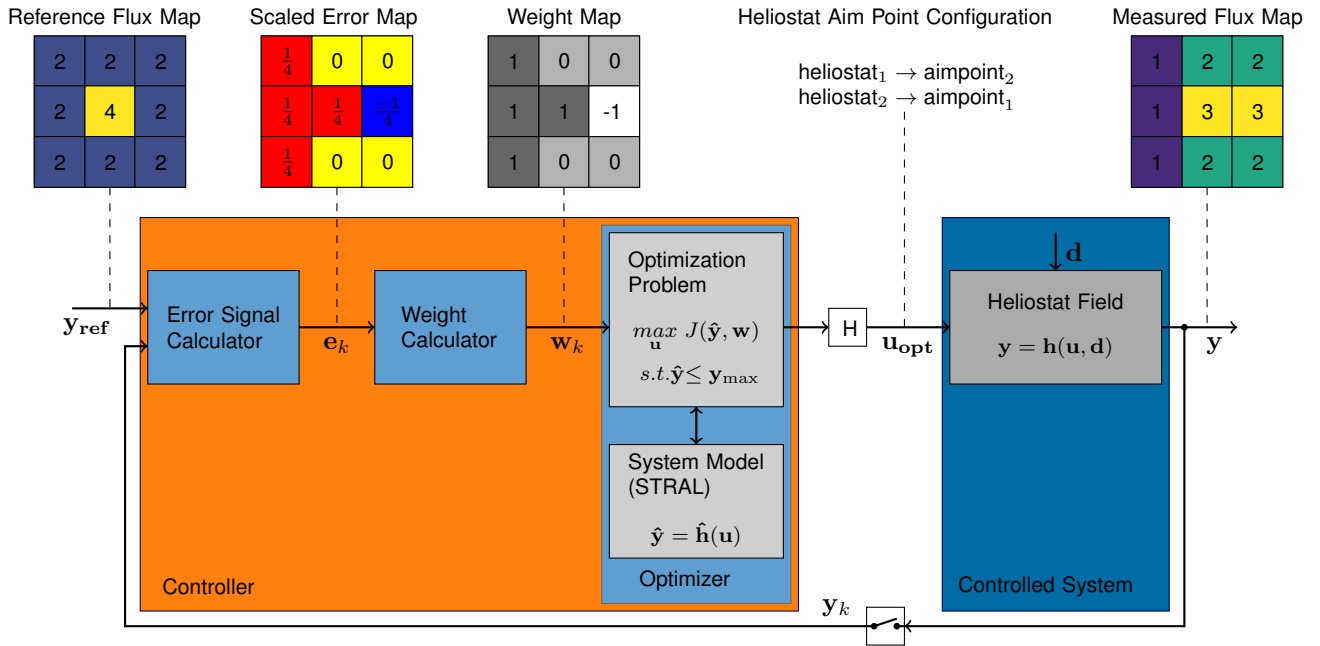
4

Figure 1: Scheme of the closed control loop comprising the Static Optimal Controller and the controlled system. An example of each signal is plotted above the loop.

sonable aim point configurations are heliostat 1 aiming to aim point 2 and heliostat 2 aiming to aim point 1 as well as heliostat 1 aiming to aim point 1 and heliostat 2 aiming to aim point 2. The first solution is chosen in the figure leading to the desired reference flux map. The second solution is worse since the spillage increases. However, it also compensates for the exceedance of the flux density.

Error Signal Calculator: First, a scaled error $\mathbf{e_{scaled}}$ is calculated from the measured flux density distribution $\mathbf{y}$ and the reference flux density distribution $\mathbf{y_{ref}}$ according to Equation (1). As the error is scaled to the maximum flux density of the reference signal, the magnitude of the error is around one. Thus, the magnitude of the weights is mostly determined by the weight calculator as desired.

$$\mathbf{e_{scaled}} = \frac{\mathbf{y_{ref}} - \mathbf{y}}{\|\mathbf{y_{ref}}\|_\infty} \qquad (1)$$

In a second step, the scaled error is shifted by a dead band d pursuant to Equation (2) leading to a shifted scaled error $\mathbf{\hat{e}_{scaled}}$.

$$\mathbf{\hat{e}_{scaled}} = \begin{cases} 0 & \text{, if } 0 \le \mathbf{e_{scaled}} \le d \\ \mathbf{e_{scaled}} - d & \text{else} \end{cases} \qquad (2)$$

By combining this shifted scaled error with an exponential term, an exponential error $\mathbf{e}$ is computed as defined in Equation (3). To adapt the impact of the exponential term, a scale factor s is included in this term.

$$\mathbf{e} = \mathbf{\hat{e}_{scaled}} \cdot e^{-s \cdot \mathbf{\hat{e}_{scaled}}} \qquad (3)$$

If the scale factor is zero, the exponential term has no impact. A scale factor below unity reduces the impact of the exponential term, while a scale factor above one enhances its effect. Figure 3 presents the exponential error as a function of the scaled error for different scale factors and dead bands.

While a negative scaled error describes an exceedance of the flux density above the reference flux density, a positive scaled error represents a flux density below the reference flux density. Hence, the exponential error is more negative if the flux density is exceeded and less positive if the flux density is undercut. Thus, exceedances of the flux density are penalized stronger, whereas flux densities below the reference flux density are rather tolerated.

The effect of the dead band is similar since it shifts the error to the right in Figure 3. Thus, negative values become even more negative and positive values become less positive. Positive errors within the range of the dead band are totally accepted as the error is set to zero. These adaptions to the scaled error reduce the risk for spots with high flux density in the flux density distribution; thus, they increase the safety of the plant. At the same time, the performance loss due to accepted flux densities slightly below the reference flux density is small.

Weight Calculator: The weight calculator used in this work is an integrator. It has the advantage to permit permanent control deviation, but it reacts rather slow. In each step, the current weight increases by the current error
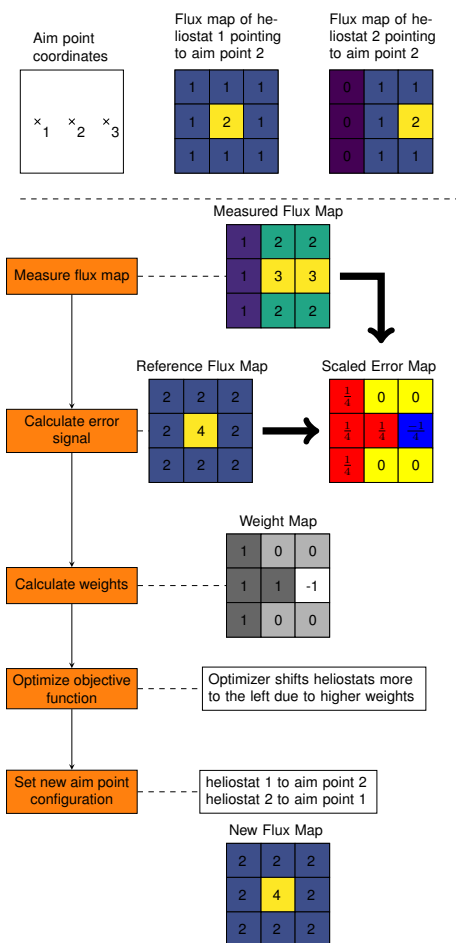
5

Figure 2: On the left hand side, the activity diagram executed in each control step of the Static Optimal Controller is presented. On the right hand side, a small example clarifying the workflow is shown.
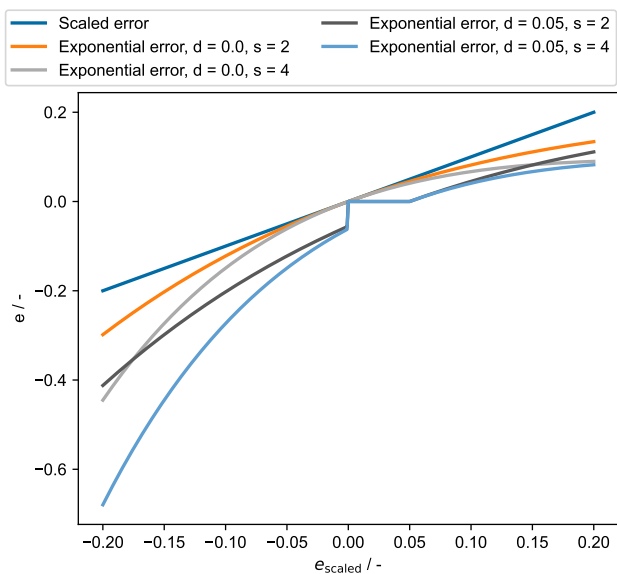

Figure 3: Exponential error in comparison to the scaled error. The exponential error is plotted for different scale factors s and dead bands d.

multiplied with the factor K_i as Equation (4) shows.

$$\mathbf{w}_{k+1} = \mathbf{w}_k + K_i \cdot \mathbf{e}_k \qquad (4)$$

To prevent divergent weights, the weight calculator is extended by an anti wind up limit.

Anti wind up: Clouds may shade parts of the heliostat field for longer periods. In consequence, the measured flux density remains below the reference flux density for longer periods of time during the operation of an SPT plant. In addition, aiming to the receiver center is more efficient than aiming close to the edges. Hence, receiver bins close to the receiver edges are often exposed to lower flux densities than the reference flux density distribution allows. This results in positive errors; consequently, the weights increase due to the integrating nature of the weight calculator. As a result, the weights diverge in the depicted scenarios. If the conditions at the SPT plant alter, a receiver bin with a diverged weight can suddenly be exposed to a high flux density. Then, many control steps are required until the weight reaches again a reasonable range. This would clearly impair the control capability of the Static Optimal Control. Hence, an anti wind up limit is included in this work.

Optimizer The included optimizer solves the optimization problem presented in Equation (5).

$$\begin{aligned} \underset{\mathbf{u}}{\text{maximize}} \quad & J(\hat{\mathbf{y}}, \mathbf{w}) \\ \text{subject to} \quad & \hat{\mathbf{y}} \le \mathbf{y}_{\max} \end{aligned} \qquad (5)$$

The underlying objective function J is maximized with respect to the simulated flux density distribution $\hat{\mathbf{y}}$ and the weights $\mathbf{w}$ by varying the aim point configuration $\mathbf{u}$. Here, the flux density distribution is simulated by the system model in STRAL. At the same time, the flux density is restricted by the AFD $\mathbf{y}_{\max}$. The length of $\mathbf{u}$ is the number of heliostats or rather groups n_{groups} and the length of all other vectors is the number of bins n_{bins}.

Objective Function: Here, the ant-colony optimization meta-heuristic (Belhomme et al., 2013) is applied as optimization algorithm maximizing the objective function. In this work, Equation (6) is applied as objective function.

$$J = \|\hat{\mathbf{y}}\|_1 - p \sum_i \max(\hat{y}_i - w_i y_{i,\max}, 0) \qquad (6)$$

Besides the flux density distribution $\hat{\mathbf{y}}$, the AFD $\mathbf{y}_{\max}$ and the weights $\mathbf{w}$ other variables like the aim point shift could be included to restrict the heliostat movement. p is the penalty factor penalizing flux density exceedances as a soft constraint.

The objective value rises if the intercepted simulated flux density increases. This is achieved by shifting heliostats to aim points with less spillage. Moreover, the AFD is scaled by an individual weight for each receiver bin. Since bins with too less flux have higher weights and bins with too much flux have lower weights, the weights allow higher irradiation if the reference flux density is not

reached. Thus, they compensate for modeling errors in the simulation. Furthermore, weights above unity give the optimizer with the opportunity to exceed the AFD with the simulated flux density without penalization. Especially in clouded scenarios, this favors higher concentrations.

Objective Value Scaler: The ACO meta-heuristic is designed for objective values between zero and unity. Since the objective function can yield negative values if the penalty term becomes large, the objective value has to be scaled. Here, Equation (7) scales each objective value towards the objective value calculated with the simulated flux from the current aim point configuration $J_{\min}$.

$$J_{\text{scaled}} = \frac{J - J_{\min}}{|J_{\min}| \cdot b} \tag{7}$$

As long as the solution of one ant is better than the current aim point configuration, the best object value is greater than zero. b denotes the improvement factor and is fitted, so that the objective value does not exceed unity. Here, $5\,\%$ are chosen.

3. Results

This section introduces first the reference power plant used for the validation of the Static Optimal Control. Subsequently, the plant is exposed to modified tracking errors. Under these conditions, the performance of the Static Optimal Control is compared the one of the DAPS. Finally, the plant is exposed to a real cloud scenario to assess if the Static Optimal Control should be used under these conditions.

3.1. Reference power plant

Since the enhancements of the ACO meta-heuristic are already studied by Oberkirsch et al. (2021) at the virtual reference power plant described by Flesch et al. (2017), the same plant is used for the evaluation of the Static Optimal Control. The plant is equipped with a cylindrical receiver and designed for a thermal power of $450\,\text{MW}$. 6482 heliostats, each with $121\,\text{m}^2$ mirror surface, concentrate this power. The initial DNI onto the cloudless heliostat field is $1000\,\text{W}\,\text{m}^{-2}$ and the evaluation is conducted on 21th of March at noon. The fixed aim point grid required for the optimization has 36 aim point in circumferential direction, 13 aim points in vertical direction and two off-receiver aim points. Thus, it has 470 aim points in total.

Flesch et al. (2017) already verified that the ACO meta-heuristic converges in combination with a thermal model of a molten salt receiver and can handle non-uniform AFDs. Hence, only the optical side of the SPT plant is considered and no thermal model is included in this work. Therefore, a constant AFD is provided to limit the flux density on the receiver's surface and the generality of the control regarding the receiver type is preserved.

3.2. Modeling errors at plant of commercial scale

This section evaluates the performance of the Static Optimal Control when compensating for static errors in the simulation model. For this reason, two SPT plant configurations are created: One models the controlled system and another one represents the system model embedded in the controller as illustrated in Figure 1. The system model assumes a mirror error of $2\,\text{mrad}$, while the controlled system exhibits a mirror error of $2.5\,\text{mrad}$ in the first test case. The Static Optimal Control is applied for 20 control steps with the controller parameters presented in Table 1. The 50 runs of the ACO meta-heuristic require with 16384 ants per run less than five seconds in each control step.

Table 1: Parameters of the Static Optimal Control and the embedded ACO meta-heuristic.

p	$\mathbf{w}_0$	K_i	s	d	n_{ants}	n_{runs}
100	1	0.5-1	2	0.05	16384	50

The initial aim point configuration is already optimized by the ACO meta-heuristic so that enhancements of the intercept can be completely attributed to the Static Optimal Control. For this, the system model exhibiting a mirror error of $2\,\text{mrad}$ is used and the AFD is $800\,\text{kW}\,\text{m}^{-2}$. The flux density distribution belonging to the found aim point configuration in combination with the model of the controlled system exhibiting a mirror error of $2.5\,\text{mrad}$ is presented in Figure 4a. Due to the increased mirror error, the flux density is clearly reduced; thus, the AFD is not reached any longer causing more spillage than necessary.

In each control step, the flux density distribution is computed with the model of the controlled system and the found aim point configuration. This flux density distribution is the feedback for the next control step of the Static Optimal Control. Based on this feedback, the controller computes the error, updates the weights and the optimizer determines a new aim point configuration based on the embedded objective function. Figure 4b shows the final weight map after 20 control steps and Figure 4c presents the final flux density distribution.

The courses of the total incident flux on the receiver and the maximum possible total incident flux are illustrated in Figure 5a. This maximum possible total flux is identified by optimizing the aim point configuration with the model of the controlled system exhibiting the mirror error of $2.5\,\text{mrad}$. During the control, the total incident flux increases from initially $98.2\,\%$ to $99.9\,\%$ of the achievable maximum.

Figure 5b illustrates the total exceeded flux as well as the maximum exceeded flux density. In three control steps, flux density exceedances above the AFD of $800\,\text{kW}\,\text{m}^{-2}$ arise. In the second control step, the highest exceedance occurs. The total exceeded flux is $11.4\,\text{kW}$ and the maximum exceeded flux density amounts to $10.5\,\text{kW}\,\text{m}^{-2}$. While the total exceeded flux corresponds to $2.4 \times 10^{-3}\,\%$

a) Initial flux map.

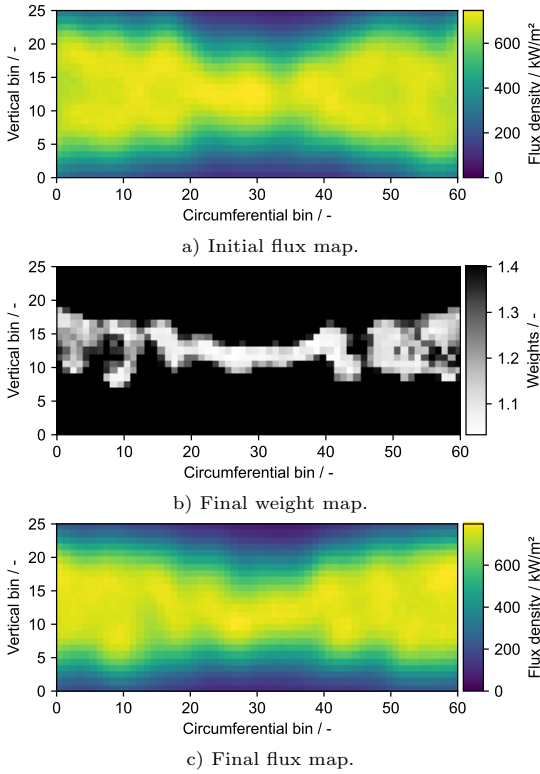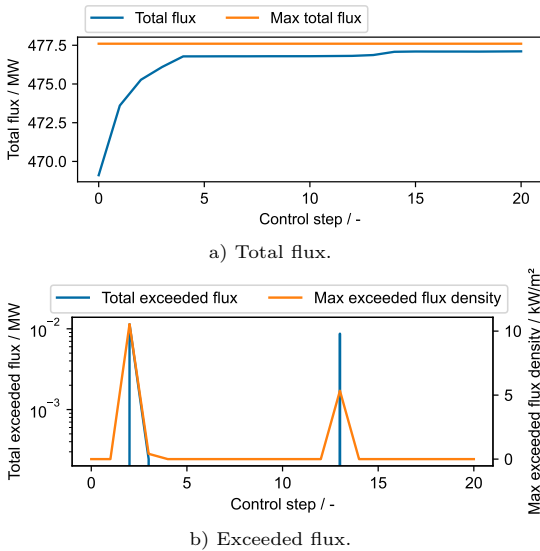

b) Final weight map.

c) Final flux map.

Figure 4: The heliostat field of the SPT plant exhibits a mirror error of 2.5 mrad while a mirror error of 2.0 mrad is incorrectly assumed in the system model of the controller. By applying aim point optimization to the system model with with a mirror error of 2.0 mrad, the initial flux map is determined. Final weight map and final flux map illustrate the final results of the Static Optimal Control after 20 control steps.

a) Initial flux map.

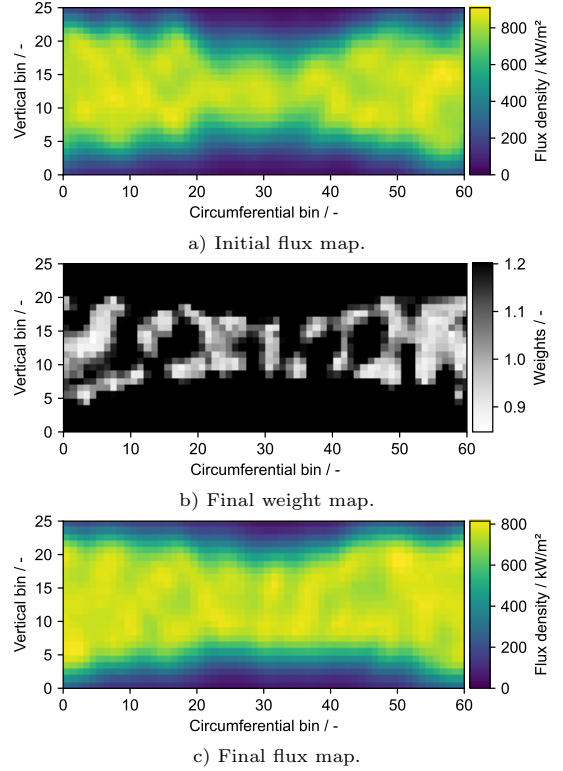b) Final weight map.

c) Final flux map.

Figure 6: The heliostat field of the SPT plant exhibits a mirror error of 1.5 mrad while a mirror error of 2.0 mrad is incorrectly assumed in the system model of the controller. By applying aim point optimization to the system model with with a mirror error of 2.0 mrad, the initial flux map is determined. Final weight map and final flux map illustrate the final results of the Static Optimal Control after 20 control steps.

a) Total flux.

b) Exceeded flux.

Figure 5: The heliostat field of the SPT plant exhibits a mirror error of 2.5 mrad while a mirror error of 2.0 mrad is incorrectly assumed in the system model of the controller. The courses of the total incident flux that is maximized by the Static Optimal Control and the maximum possible incident flux are presented in subfigure Figure 5a. In subfigure Figure 5b, the emerging total exceeded flux and the maximum exceeded flux density are shown.

of the total flux, the maximum exceeded flux density is 1.3 % of the AFD.

In the second test case, the mirror error of the model representing the controlled system reduces to 1.5 mrad, while the system model within the optimizer remains the same with a mirror error of 2 mrad. Once again, the control starts from the aim point configuration optimized by the ACO meta-heuristic based on the system model. Due to the lower mirror error in the controlled system, this aim point configuration causes flux density exceedances in this case. In the receiver bins around the equatorial line of the receiver, a maximum flux density of $910\,\mathrm{kW\,m^{-2}}$ occurs as Figure 6a illustrates. Hence, the AFD of $800\,\mathrm{kW\,m^{-2}}$ is clearly exceeded. In consequence, the weights are adapted based on the flux density feedback resulting after 20 control steps in the weight map pictured in Figure 6b. Compared to Figure 6a, the final flux density distribution achieved by the Static Optimal Control is clearly widened as Figure 6c illustrates. The corresponding maximum flux density amounts to $814\,\mathrm{kW\,m^{-2}}$ and is thus considerably closer to the AFD.

The courses of the total incident flux and the achievable maximum total incident flux are shown for the 20 control steps in Figure 7a. The maximum possible total incident
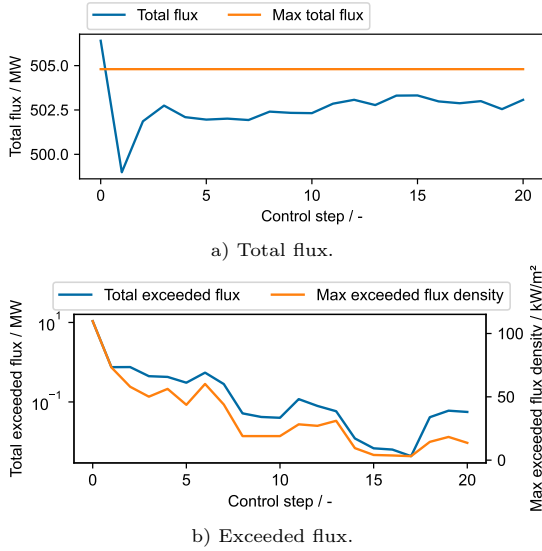
8

a) Total flux.

b) Exceeded flux.

Figure 7: The heliostat field of the SPT plant exhibits a mirror error of 1.5 mrad while a mirror error of 2.0 mrad is incorrectly assumed in the system model of the controller. The courses of the total incident flux that is maximized by the Static Optimal Control and the maximum possible incident flux are presented in subfigure Figure 7a. In subfigure Figure 7b, the emerging total exceeded flux and the maximum exceeded flux density are shown.

a) Comparison DAPS and static optimal control.

b) Final flux map DAPS.
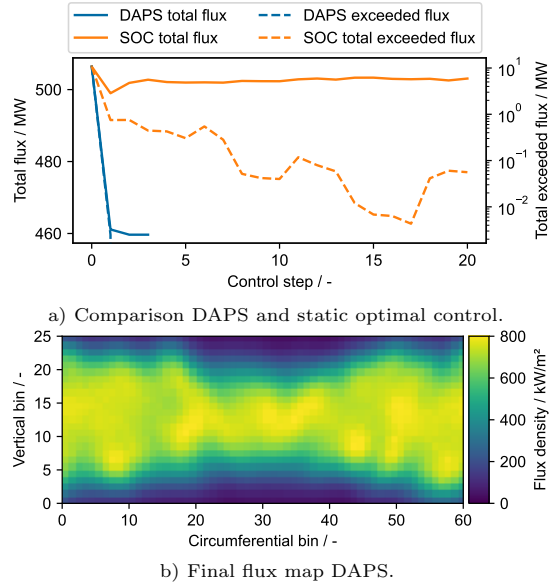
Figure 8: Controlling an SPT plant with a mirror error of 1.5 mrad while assuming incorrectly a mirror error of 2.0 mrad in the simulation model of the controller. The control starts from the optimized aim point configuration using a simulation model with a mirror error of 2.0 mrad. Both, the DAPS and the static optimal control reduce the exceeded flux as presented in Figure 8a. At the same time, the static optimal control maximizes the total intercept power on the receiver. Additionally, the final flux map achieved by the DAPS is shown in Figure 8b.

flux is once again determined by the ACO meta-heuristic and the model of the controlled system. The system model exhibits a mirror error of 1.5 mrad in this case. The total incident flux even exceeds the achievable maximum. However, the flux density exceeds opposed to the solution with the maximum possible incident flux also the AFD.

The course of the exceeded flux as it is compensated for by the Static Optimal Control is illustrated in Figure 7b. To accomplish the reduction of the total exceeded flux by 93 % in the first control step, the total flux drops as well. However, while the total exceeded flux reduces by over 9 MW, the total flux only declines by less than 8 MW. In control steps two and three, the Static Optimal Control increases the total flux by 0.7 % while the remaining total exceeded flux halves once again. After 20 control steps, the total incident flux reaches 99.6 % of the achievable maximum. In this control step, the total exceeded flux amounts to 0.08 % of the total incident flux and the AFD is exceeded by maximally 14.4 kW m^{-2} corresponding to 1.8 % of the AFD.

After the performance of the Static Optimal Control is assessed individually, it is compared to the DAPS (Vant-Hull et al., 1996a) in the following. For this first test case, a comparison is not totally possible since the DAPS can only compensate for flux density exceedances but cannot enhance the total incident flux. Hence, the controller would not react and the total incident flux would remain at the initial 98.2 % of the achievable maximum. However, the comparison between Static Optimal Control and DAPS is possible for the second test case and the results are shown in Figure 8.

As Figure 8a demonstrates, the DAPS compensates within two control steps for the flux density exceedances. For this, the DAPS determines all heliostats that cause based on the system model with a mirror error of 2.0 mrad flux density exceedances and removes these heliostats from tracking. As the system model deviates from the model of the controlled system with a mirror error of 1.5 mrad, the concentration is slightly higher than expected. Therefore, the DAPS requires a second control step.

In this way, the DAPS eliminates all exceedances of the flux density, whereas flux density exceedances remain when applying the Static Optimal Control. However, the DAPS causes a performance loss of roughly 9 % compared to the maximum achievable total flux, while the performance loss coming along with the Static Optimal Control is only 0.4 %.

The flux density distribution belonging to the solution found by the DAPS after two control steps is presented in Figure 8b. The DAPS does not reallocate the heliostats on the receiver like the Static Optimal Control. Instead, it removes the heliostats completely from tracking the receiver. Hence, the flux density distribution is not widened. The power of these heliostats is lost instead of being received by sections closer to the receiver edges. This is in contrast to the solution found by the Static Optimal Control illustrated in Figure 6c.
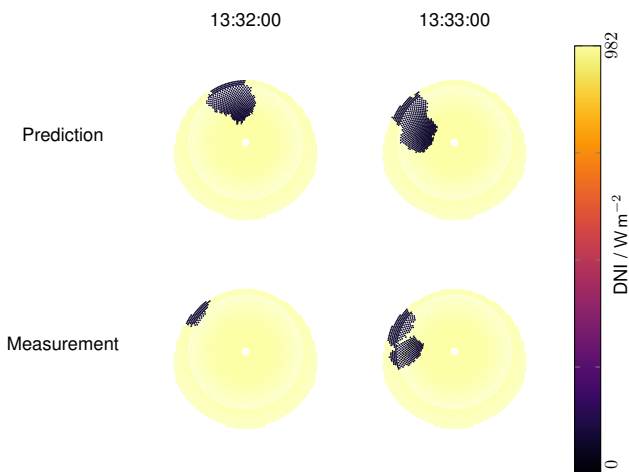
Figure 9: A real cloud scenario is presented. For this, real DNI predictions made by the ASI-based nowcasting system described by Nouri et al. (2020) are mapped onto the heliostat field of the reference power plant introduced in Section 3.1. The predictions made one minute ahead are presented on the upper half of the figure and the measurements are illustrated on the lower half of the figure. The time of prediction and measurement is indicated above each column.
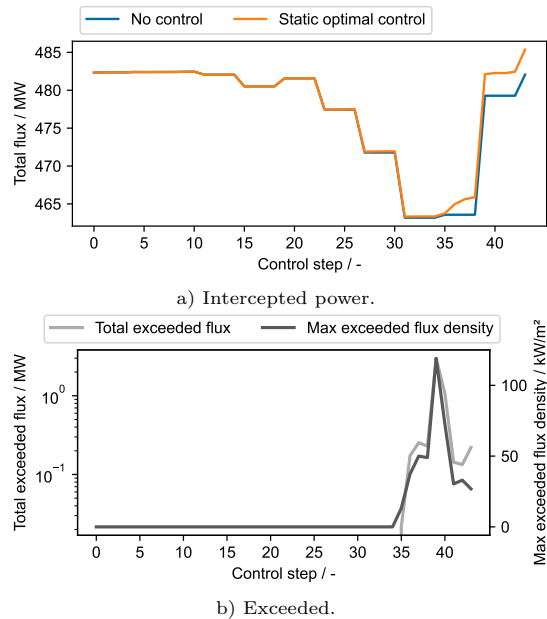
3.3. Disturbances at plant of commercial scale

On the one hand, deviations between system model and the controlled system exist in the control of SPT plants. On the other hand, these plants are exposed to disturbances caused by clouds. Hence, the Static Optimal Control should not only compensate for modeling errors, but also reject these dynamic disturbances. Hence, the reference power plant presented in Section 3.1 is exposed to a clouded scenario in the following to assess the performance of the Static Optimal Control.

For this reason, a real clouded scenario recorded by an ASI-based nowcasting system (Nouri et al., 2018, 2019, 2020) is superimposed on the heliostat field of the reference power plant. Therefore, the power of each heliostat is scaled by the DNI measured at its position. The clouded scenario has a total duration of five minutes. It starts at 13:29:00 and finishes at 13:34:00. In this clouded scenario, clear sky conditions prevail at the beginning, before a small cloud passes the heliostat field. Figure 9 illustrates the measurements for 13:32:00 and 13:33:00. Furthermore, two predictions of the ASI-based nowcasting system are presented in this figure. As the lead time of these nowcasts is one minute, they are predicted at 13:31:00 and 13:32:00 for one minute ahead.

According to Oberkirsch et al. (2021), the optimization duration for 50 ants is roughly 5 s at the reference power plant. Moreover, the temporal resolution of the nowcasting system is 30 s. In this study, four control steps should be applied until the DNI situation is varied based on a new measurement. This gives the heliostats according to Equation (8) 2.5 s to move.

a) Intercepted power.

b) Exceeded.

Figure 10: Controlling an SPT plant with a mirror error of 2.0 mrad exposed to cloud disturbances. A real cloud measurement is applied and the cloud moves every fourth control step.

$$t_{\text{move}} = \frac{t_{\text{step}}}{steps} - t_{\text{optimization}} = \frac{30\,\text{s}}{4} - 5\,\text{s} = 2.5\,\text{s} \quad (8)$$

Figure 10 presents the courses of the total incident flux and the total exceeded flux on the receiver. For comparison, Figure 10a shows the total incident flux on the one hand using the Static Optimal Control and on the other hand without any control. In the case without any control, the optimized aim point configuration for the clear sky scenario is applied and not varied during the entire test period. Hence, the heliostats are not reallocated as soon as the DNI above the heliostat field drops due to the clouds.

In contrast, the Static Optimal Control adapts the aim point configuration in control step 35 for the first time to reduce spillage. This indicates Figure 10a. Prior to control step 35, the weights did not adjust sufficiently strong to justify changing the aim point configuration. The weights adjust slowly as the cloud is little; thus, it causes only a small error between reference and measured flux density distribution. By the end of the clouded scenario, the Static Optimal Control increases the total incident flux by 0.6 %.

However, the Static Optimal Control leads at the same time to a total exceeded flux of 3 MW in control step 39. This corresponds to 0.6 % of the total incident flux as Figure 10b illustrates. The maximum exceeded flux density arises with 119 kW m^{-2} also in control step 39.

Besides measuring the current DNI, the ASI-based nowcasting system predicts also the emerging DNI for the future. Hence, these predicted DNI information is superimposed to the system model used in the controller. Here, the minimum available lead time of one minute is applied.
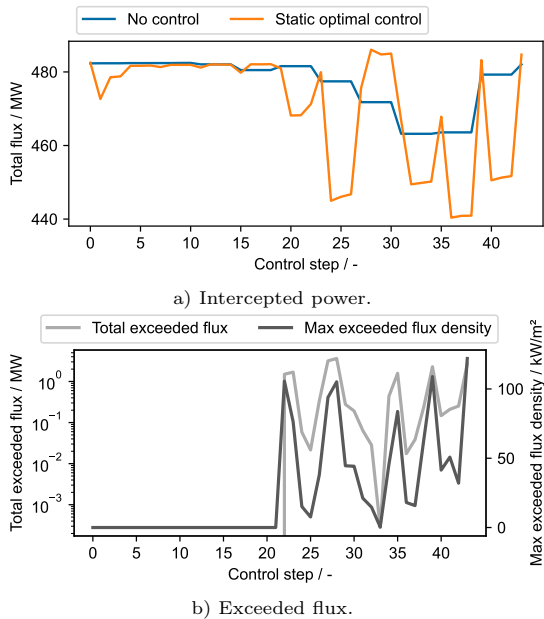
a) Intercepted power.

b) Exceeded flux.

Figure 11: Controlling an SPT plant with a mirror error of 2.0 mrad, exposed to cloud disturbances. A real cloud measurement is applied and the cloud moves every fourth control step. Additionally, the controller receives the prediction of the DNI with a lead time of one minute in a feed forward manner.

By using the nowcasting data, the Static Optimal Control receives information about occurring clouds directly in a feed forward way. This is in contrast to the previous simulations, where the Static Optimal Control only received indirect information about the clouds through the flux density feedback. Figure 11 presents the results of the Static Optimal Control under these conditions.

Compared to the results without any control, the total incident flux fluctuates strongly as Figure 11a illustrates. Figure 11b indicates that the flux density exceeds the AFD already in control step 22. The maximum exceeded flux density is $122 \, \mathrm{kW \, m^{-2}}$ and the total exceeded flux amounts to 3.6 MW.

4. Discussion

The Static Optimal Control demonstrated in Section 3.2 that it is able to compensate for static modeling errors at a plant of commercial scale. The first test case analyzed a scenario with an increased mirror error in the controlled system. There, the control improved the intercept by 1.7 % in comparison to the DAPS or aim point optimization. At the same time, the flux density exceeds the AFD by maximally 1.3 %. Thus, the defined aim of 5 % is reached and the exceedances are clearly below the accuracy of the flux density measurement system.

In a second scenario, the mirror error is reduced by 0.5 mrad in the controlled system. There, the Static Optimal Control reduces already in the first control step the total exceeded flux by 93 %. After the second control step, the maximally emerging flux density exceedance declined

to around $50 \, \mathrm{kW \, m^{-2}}$ (6.25 %). In the eighth control step, the maximum flux density exceedances drops below the defined target level of 5 %. The final maximum exceedance of the AFD is 1.8 % after 20 control steps. Hence, the Static Optimal Control fulfills the aim of a maximum exceedance of 5 % above the AFD when compensating for static modeling errors. In contrast, the exceedances above the AFD remain using an open-loop control. The DAPS, in turn, completely eliminates the flux density exceedances. However, the DAPS looses 9 % of the maximum achievable intercept reasoned in the defocusing of the heliostats. In comparison, the Static Optimal Control forfeits only 0.4 % of this maximum.

In Section 3.3, the performance of the Static Optimal Control is studied at a plant of commercial scale under disturbances due to a small cloud. The variations in the DNI cause oscillations in the weight map and, in turn, clear exceedances above the AFD. Even though the $150 \, \mathrm{kW \, m^{-2}}$-tolerance range stated by Gross et al. (2020) is observed, the defined aim of 5 % above the AFD could not be met as the maximum exceedance is $122 \, \mathrm{kW \, m^{-2}}$ (15.25 %). Thus, the Static Optimal Control is with the currently selected controller settings not suited to reject dynamic disturbances. For more extensive tests, other objective functions should be tested as they have already proven in simplified tests that they eliminate flux exceedances better.

In a subsequent step, the Static Optimal Control is extended by a feed forward control. For this, DNI predictions with a lead time of 1 min have been applied. However, even this feed forward control did not prevent the oscillating spots in the flux density distribution since the predicted clouds were bigger than the ones that actually occurred as Figure 9 illustrates. In consequence of too large predicted clouds, the Static Optimal Control shifted the heliostats to the receiver equator for spillage reduction. At these equatorial regions, the ultimately higher DNI results in flux density exceedances. This amplifies the oscillating spots in the flux density distribution further instead of damping them.

Hence, the accuracy of the ASI-based nowcasting system is not suited to improve the Static Optimal Control under these dynamic conditions. In the future, the accuracy of the nowcasting system has to be improved. Alternatively, Nouri et al. (2019) determine additional DNI maps that only reduce the DNI at positions that have a significantly higher chance to be shaded. Using these uncertainty maps, reduces clearly the probability of concentrating too much onto the receiver center. In combination with the adapted controller settings, this could be a way to handle the emerging oscillating spots in the flux density distribution under transient DNI conditions.

5. Conclusion

In this paper, the Static Optimal Control is proposed as a closed-loop aim point control technique for solar power tower plants. The Static Optimal Control assumes a static

system; thus, the sample time of the control has to be selected longer than the maximum heliostat movement within one control step. The heart of the Static Optimal Control is the embedded optimizer. This optimizer finds optimal solutions regarding an objective function and makes the control stand off among other existing closed-loop aim point control techniques.

The flux density feedback is recorded directly by a flux density measurement system. An error signal calculator compares this feedback with the reference flux density and a weight calculator estimates weights based on the error signal. These weights are included in the objective function of the optimizer. In this way, the Static Optimal Control compensates for static modeling errors in the system model. In two investigated test cases, it enhances the performance of a plant of commercial scale by 1.7-8.6 % in comparison to the *Dynamic Aimpoint Processing System* (DAPS) (Vant-Hull et al., 1996a) as reference approach. Under a real cloud scenario, the Static Optimal Control reaches its limits as the flux density exceeds the AFD by maximally 15.25 %. Here, more conservative objective functions have to be studied. Scaling the power of the heliostats by the predicted DNI of a nowcasting system in a feed forward manner, does not enhance the control quality since the accuracy of the nowcasts is not sufficient.

In the future, nowcasting maps that only reduce the DNI in regions that have a high probability to be shaded will be applied for the feed forward control and more conservative controller settings will be investigated for the Static Optimal Control. In this way, the oscillating flux density spots under transient conditions should be prevented. Furthermore, this closed-loop control will be embedded in an aim point management system. This overall system detects scenarios, where the control can be applied safely. In the remaining transient scenarios, more conservative control approaches are used. Finally, this system including the Static Optimal Control will be validated at the Jülich solar tower.

Acknowledgement

References

L. Vant-Hull, M. Izygon, C. Pitman, B. Wilkins-Crowder, R. Campbell-Howe, Real-Time Computation and Control of Solar Flux Density on a Central Receiver (Solar Two) (Protection Against Excess Flux Density), in: American Solar Energy Society, SOLAR -ANNUAL MEETING- AMERICAN SOLAR ENERGY SOCIETY-, ASES;, Boulder, CO, 1996a, pp. 88–94. URL: https://www.tib.eu/de/suchen/id/BLCP%3ACN017157193.

L. L. Vant-Hull, M. E. Izygon, C. L. Pitman, J. H. Davidson, J. Chavez, Real-Time Computational and Control of Solar Flux Density on a Central Receiver (Solar Two) (Preheat), in: International Solar Energy Conference, ASME;, 1996b, pp. 139–142. URL: https://www.tib.eu/de/suchen/id/BLCP%3ACN015836374.

D. C. Smith, Design and optimization of tube-type receiver panels for molten salt application, Solar Engineering 2 (1992) 1029–1036.

R. W. Bradshaw, D. B. Dawson, W. De la Rosa, R. GILBERT, S. H. GOODS, M. J. HALE, P. JACOBS, S. A. JONES, G. J. KOLB, J. E. PACHECO, M. R. PRAIRIE, H. E. REILLY, S. K. SHOWALTER, L. L. VANT-HULL, Final Test and Evaluation Results from the Solar Two Project (2002). URL: https://www.osti.gov/biblio/793226. doi:10.2172/793226.

L. L. Vant-Hull, The Role of "Allowable Flux Density" in the Design and Operation of Molten-Salt Solar Central Receivers , Journal of Solar Energy Engineering 124 (2002) 165–169. URL: https://doi.org/10.1115/1.1464124. doi:10.1115/1.1464124.

A. Sánchez-González, D. Santana, Solar flux distribution on central receivers: A projection method from analytic function, Renewable Energy 74 (2015) 576 – 587. URL: http://www.sciencedirect.com/science/article/pii/S0960148114004753. doi:https://doi.org/10.1016/j.renene.2014.08.016.

A. Sánchez-González, M. R. Rodríguez-Sánchez, D. Santana, Aiming strategy model based on allowable flux densities for molten salt central receivers, Solar Energy 157 (2017) 1130 – 1144. URL: http://www.sciencedirect.com/science/article/pii/S0038092X16001468. doi:https://doi.org/10.1016/j.solener.2015.12.055.

A. Sánchez-González, M. R. Rodríguez-Sánchez, D. Santana, Aiming factor to flatten the flux distribution on cylindrical receivers, Energy 153 (2018) 113 – 125. URL: http://www.sciencedirect.com/science/article/pii/S0360544218305929. doi:https://doi.org/10.1016/j.energy.2018.04.002.

R. Flesch, C. Frantz, D. M. Quinto, P. Schwarzbözl, Towards an optimal aiming for molten salt power towers, Solar Energy 155 (2017) 1273 – 1281. URL: http://www.sciencedirect.com/science/article/pii/S0038092X17306527. doi:https://doi.org/10.1016/j.solener.2017.07.067.

F. J. Collado, J. Guallar, A two-parameter aiming strategy to reduce and flatten the flux map in solar power tower plants, Solar Energy 188 (2019) 185 – 189. URL: http://www.sciencedirect.com/science/article/pii/S0038092X19305663. doi:https://doi.org/10.1016/j.solener.2019.06.001.

M. Astolfi, M. Binotti, S. Mazzola, L. Zanellato, G. Manzolini, Heliostat aiming point optimization for external tower receiver, Solar Energy 157 (2017) 1114 – 1129. URL: http://www.sciencedirect.com/science/article/pii/S0038092X16002292. doi:https://doi.org/10.1016/j.solener.2016.03.042.

J. García, Y. C. Soo Too, R. Vasquez Padilla, R. Barraza Vicencio, A. Beath, M. Sanjuan, Heat flux distribution over a solar central receiver using an aiming strategy based on a conventional closed control loop, in: ASME 2017 11th International Conference on Energy Sustainability, Energy Sustainability, 2017. URL: https://doi.org/10.1115/ES2017-3615. doi:10.1115/ES2017-3615.

A. Salomé, F. Chhel, G. Flamant, A. Ferrière, F. Thiery, Control of the flux distribution on a solar tower receiver using an optimized aiming point strategy: Application to THEMIS solar tower, Solar Energy 94 (2013) 352 – 366. URL: http://www.sciencedirect.com/science/article/pii/S0038092X1300090X. doi:https://doi.org/10.1016/j.solener.2013.02.025.

Q. Yu, Z. Wang, E. Xu, Analysis and improvement of solar flux distribution inside a cavity receiver based on multi-focal points of heliostat field, Applied Energy 136 (2014) 417 – 430. URL: http://www.sciencedirect.com/science/article/pii/S0306261914009556. doi:https://doi.org/10.1016/j.apenergy.2014.09.008.

B. Grange, G. Flamant, Aiming Strategy on a Prototype-Scale Solar Receiver: Coupling of Tabu Search, Ray-Tracing and Thermal Models, Sustainability 13 (2021). URL: https://www.mdpi.com/2071-1050/13/7/3920. doi:10.3390/su13073920.

S. M. Besarati, D. Y. Goswami, E. K. Stefanakos, Optimal

heliostat aiming strategy for uniform distribution of heat flux on the receiver of a solar power tower plant, Energy Conversion and Management 84 (2014) 234 – 243. URL: http://www.sciencedirect.com/science/article/pii/S0196890414003343. doi:https://doi.org/10.1016/j.enconman.2014.04.030.

K. Wang, Y.-L. He, X.-D. Xue, B.-C. Du, Multi-objective optimization of the aiming strategy for the solar power tower with a cavity receiver by using the non-dominated sorting genetic algorithm, Applied Energy 205 (2017) 399 – 416. URL: http://www.sciencedirect.com/science/article/pii/S0306261917309698. doi:https://doi.org/10.1016/j.apenergy.2017.07.096.

N. Cruz, J. Álvarez, J. Redondo, M. Berenguel, P. Ortigosa, A two-layered solution for automatic heliostat aiming, Engineering Applications of Artificial Intelligence 72 (2018) 253–266. URL: https://www.sciencedirect.com/science/article/pii/S0952197618300939. doi:https://doi.org/10.1016/j.engappai.2018.04.014.

N. C. Cruz, J. Domingo Álvarez, J. L. Redondo, M. Berenguel, P. M. Ortigosa, R. Klempous, Control and optimal management of a heliostat field for solar power tower systems, in: 2019 IEEE 23rd International Conference on Intelligent Engineering Systems (INES), 2019, pp. 000271–000274. doi:10.1109/INES46365.2019.9109493.

R. Zhu, D. Ni, An Optimized Aiming Strategy Tracking Flux Set Point for Solar Power Tower System, in: 2019 Chinese Automation Congress (CAC), 2019, pp. 1386–1391. doi:10.1109/CAC48633.2019.8996344.

H. Kellerer, U. Pferschy, D. Pisinger, Multidimensional Knapsack Problems, Springer Berlin Heidelberg, Berlin, Heidelberg, 2004, pp. 235–283. URL: https://doi.org/10.1007/978-3-540-24777-7_9. doi:10.1007/978-3-540-24777-7_9.

T. Ashley, E. Carrizosa, E. Fernández-Cara, Optimisation of aiming strategies in solar power tower plants, Energy 137 (2017) 285 – 291. URL: http://www.sciencedirect.com/science/article/pii/S0360544217311581. doi:https://doi.org/10.1016/j.energy.2017.06.163.

P. Richter, F. Kepp, C. Büsing, S. Kuhnke, Optimization of robust aiming strategies in solar tower power plants, AIP Conference Proceedings 2126 (2019) 030045. URL: https://aip.scitation.org/doi/abs/10.1063/1.5117557. doi:10.1063/1.5117557. arXiv:https://aip.scitation.org/doi/pdf/10.1063/1.5117557.

S. Kuhnke, P. Richter, F. Kepp, J. Cumpston, A. M. Koster, C. Büsing, Robust optimal aiming strategies in central receiver systems, Renewable Energy 152 (2020) 198 – 207. URL: http://www.sciencedirect.com/science/article/pii/S0960148119318129. doi:https://doi.org/10.1016/j.renene.2019.11.118.

N. Speetzen, P. Richter, Dynamic aiming strategy for central receiver systems, Renewable Energy 180 (2021) 55–67. URL: https://www.sciencedirect.com/science/article/pii/S0960148121012209. doi:https://doi.org/10.1016/j.renene.2021.08.060.

B. Belhomme, R. Pitz-Paal, P. Schwarzbözl, Optimization of Heliostat Aim Point Selection for Central Receiver Systems Based on the Ant Colony Optimization Metaheuristic, Journal of Solar Energy Engineering 136 (2013). URL: https://doi.org/10.1115/1.4024738. doi:10.1115/1.4024738.

D. Maldonado, R. Flesch, A. Reinholz, P. Schwarzbözl, Evaluation of aim point optimization methods, AIP Conference Proceedings 2033 (2018) 040025. URL: https://aip.scitation.org/doi/abs/10.1063/1.5067061. doi:10.1063/1.5067061.

L. Oberkirsch, D. Maldonado Quinto, P. Schwarzbözl, B. Hoffschmidt, Gpu-based aim point optimization for solar tower power plants, Solar Energy (2021). URL: https://www.sciencedirect.com/science/article/pii/S0038092X20312123. doi:https://doi.org/10.1016/j.solener.2020.11.053.

P. Kuhn, M. Wirtz, S. Wilbert, J. Bosch, G. Wang, L. Ramirez, D. Heinemann, R. Pitz-Paal, Field validation and benchmarking of a cloud shadow speed sensor, Solar Energy 173 (2018) 229–245.

B. Nouri, P. Kuhn, S. Wilbert, C. Prahl, R. Pitz-Paal, P. Blanc, T. Schmidt, Z. Yasser, L. R. Santigosa, D. Heineman, Nowcasting of DNI maps for the solar field based on voxel carving and individual 3D cloud objects from all sky images, AIP Conference Proceedings 2033 (2018) 190011. doi:10.1063/1.5067196.

B. Nouri, S. Wilbert, P. Kuhn, N. Hanrieder, M. Schroedter-Homscheidt, A. Kazantzidis, L. Zarzalejo, P. Blanc, S. Kumar, N. Goswami, R. Shankar, R. Affolter, R. Pitz-Paal, Real-time uncertainty specification of all sky imager derived irradiance nowcasts, Remote Sensing 11 (2019) 1059. doi:10.3390/rs11091059.

B. Nouri, K. Noureldin, T. Schlichting, S. Wilbert, T. Hirsch, M. Schroedter-Homscheidt, P. Kuhn, A. Kazantzidis, L. Zarzalejo, P. Blanc, Z. Yasser, J. Fernández, R. Pitz-Paal, Optimization of parabolic trough power plant operations in variable irradiance conditions using all sky imagers, Solar Energy 198 (2020) 434–453. doi:10.1016/j.solener.2020.01.045.

N. Cruz, J. Álvarez, J. Redondo, M. Berenguel, R. Klempous, P. Ortigosa, A Simple and Effective Heuristic Control System for the Heliostat Field of Solar Power Tower Plants, Acta Polytechnica Hungarica 17 (2020) 7–26. doi:10.12700/APH.17.4.2020.4.1.

F. García-Martín, M. Berenguel, A. Valverde, E. Camacho, Heuristic knowledge-based heliostat field control for the optimization of the temperature distribution in a volumetric receiver, Solar Energy 66 (1999) 355 – 369. URL: http://www.sciencedirect.com/science/article/pii/S0038092X99000249. doi:https://doi.org/10.1016/S0038-092X(99)00024-9.

J. García, Y. Chean Soo Too, R. Vasquez Padilla, A. Beath, J.-S. Kim, M. E. Sanjuan, Multivariable Closed Control Loop Methodology for Heliostat Aiming Manipulation in Solar Central Receiver Systems, Journal of Solar Energy Engineering 140 (2018). URL: https://doi.org/10.1115/1.4039255. doi:10.1115/1.4039255, 031010.

D. Acosta, J. Garcia, M. Sanjuan, L. Oberkirsch, P. Schwarzbözl, Flux-feedback as a fast alternative to control groups of aiming points in molten salt power towers, Solar Energy 215 (2021) 12–25. URL: https://www.sciencedirect.com/science/article/pii/S0038092X20312792. doi:https://doi.org/10.1016/j.solener.2020.12.028.

P. Schwarzbözl, R. Pitz-Paal, M. Schmitz, Visual hflcal-a software tool for layout and optimisation of heliostat fields, in: Proceedings, 2009.

J. García, Y. C. Soo Too, R. Padilla, A. Beath, j.-s. Kim, M. Sanjuan, Dynamic performance of an aiming control methodology for solar central receivers due to cloud disturbances, Renewable Energy 121 (2018) 355–367. doi:10.1016/j.renene.2018.01.019.

Y. C. Soo Too, J. García, R. V. Padilla, J.-S. Kim, M. Sanjuan, A transient optical-thermal model with dynamic matrix controller for solar central receivers, Applied Thermal Engineering 154 (2019) 686 – 698. URL: http://www.sciencedirect.com/science/article/pii/S1359431118370327. doi:https://doi.org/10.1016/j.applthermaleng.2019.03.086.

J. García, R. Barraza, Y. C. Soo Too, R. Vásquez Padilla, D. Acosta, D. Estay, P. Valdivia, Aiming clusters of heliostats over solar receivers for distributing heat flux using one variable per group, Renewable Energy 160 (2020) 584–596. URL: https://www.sciencedirect.com/science/article/pii/S0960148120310107. doi:https://doi.org/10.1016/j.renene.2020.06.096.

J. García, R. Barraza, Y. C. Soo Too, R. Vásquez Padilla, D. Acosta, D. Estay, P. Valdivia, Tuning Analysis and Optimization of a Cluster-Based Aiming Methodology for Solar Central Receivers, Frontiers in Energy Research 10 (2022). URL: https://www.frontiersin.org/article/10.3389/fenrg.2022.808816. doi:10.3389/fenrg.2022.808816.

F. Gross, W. A. Landman, M. Balz, D. Sun, Robust aim point strategy for dynamic solar tower plant operation, AIP Conference Proceedings 2303 (2020) 030018. URL: https://aip.scitation.org/doi/abs/10.1063/5.0028941. doi:10.1063/5.0028941. arXiv:https://aip.scitation.org/doi/pdf/10.1063/5.0028941.

M. Röger, P. Herrmann, S. Ulmer, M. Ebert, C. Prahl, F. Göhring, Techniques to Measure Solar Flux Density Distribution on Large-Scale Receivers, Journal of Solar Energy Engineering 136 (2014). URL: https://doi.org/10.1115/1.4027261. doi:10.1115/1.4027261, 031013.

M. Offergeld, M. Röger, H. Stadler, P. Gorzalka, B. Hoffschmidt, Flux density measurement for industrial-scale solar power towers using the reflection off the absorber, in: AIP Conference Proceedings, volume 2126, AIP Publishing LLC, 2019, p. 110002.

F. Göhring, O. Bender, M. Röger, J. Nettlau, P. Schwarzbözl, Flux density measurement on open volumetric receivers, 2011.

H. Stadler, D. Maldonado, M. Offergeld, P. Schwarzbözl, J. Trautner, CFD model for the performance estimation of open volumetric receivers and comparison with experimental data, Solar Energy 177 (2019) 634–641. URL: https://www.sciencedirect.com/science/article/pii/S0038092X18311757. doi:https://doi.org/10.1016/j.solener.2018.11.068.

B. Belhomme, R. Pitz-Paal, P. Schwarzbözl, S. Ulmer, A New Fast Ray Tracing Tool for High-Precision Simulation of Heliostat Fields, Journal of Solar Energy Engineering 131 (2009). URL: https://doi.org/10.1115/1.3139139. doi:10.1115/1.3139139.

S. Lloyd, Least squares quantization in PCM, IEEE Transactions on Information Theory 28 (1982) 129–137. doi:10.1109/TIT.1982.1056489.

NVIDIA Corporation, NVIDIA CUDA C++ Programming Guide, 2019. URL: https://docs.nvidia.com/cuda/pdf/CUDA_C_Programming_Guide.pdf.

SENER, CPV & CSP TWO AXES SOLAR TRACKER, 2014. URL: http://www.sener-power-process.com/EPORTAL_DOCS/GENERAL/SENERV2/DOC-cw499d8e0908599/CPVCSPtwoaxessolartracker.pdf.